



Ultrafast laser-inscribed mid-infrared evanescent field directional couplers in GeAsSe chalcogenide glass

HELEN L. BUTCHER,¹ DAVID G. MACLACHLAN,² DAVID LEE,³ ROBERT R. THOMSON,² AND DAMIEN WEIDMANN^{1,*}

¹Space Science and Technology Department (RAL Space), STFC Rutherford Appleton Laboratory, Harwell Campus, Didcot, OX11 0QX, UK

²Scottish Universities Physics Alliance (SUPA), Institute of Photonics and Quantum Sciences, School of Engineering and Physical Sciences, David Brewster Building, Heriot Watt University, Edinburgh, EH14 4AS, UK

³Science and Technology Facilities Council, UK Astronomy Technology Centre, Blackford Hill, Edinburgh, EH9 3HJ, UK

*damiem.weidmann@stfc.ac.uk

Abstract: Mid-infrared evanescent field directional couplers operating at $\sim 8 \mu\text{m}$ are demonstrated by ultrafast laser inscription of waveguides in $\text{Ge}_{33}\text{As}_{12}\text{Se}_{55}$ (IG2) chalcogenide glass. Through-port coupling ratios from $> 99:1$ to $< 1:99$ were observed, and comparison of the measured devices to analytic and numeric models verifies device performance against theory. Insertion loss of the couplers is estimated to be 0.9 dB, in addition to approximately 1 dB/cm propagation loss. These couplers are developed to enable more complex mid-infrared, and particularly the long wave infrared, ultrafast laser-inscribed photonics components, such as integrated Mach-Zehnder interferometers and photonic lanterns, to be realized in future.

Published by The Optical Society under the terms of the [Creative Commons Attribution 4.0 License](https://creativecommons.org/licenses/by/4.0/). Further distribution of this work must maintain attribution to the author(s) and the published article's title, journal citation, and DOI.

1. Introduction

Integrated optics (IO) in the infrared (IR) portion of the electromagnetic spectrum has received much attention over recent years, owing to the success of silica-based IO components for telecommunications [1] and refractive index sensing devices [2] in the near-IR spectral region. Part of the success of these components is due to the mature IO ‘toolbox’ available in this material, which includes passive components such as integrated waveguides and beam combiners [3]; these functions are combined on a single chip to create complex photonics devices.

The mid-IR portion of the spectrum (2–20 μm) is advantageous for applications such as integrated sensing [4], molecular spectroscopy [5], and astrophotonics [6], due to the presence of strong fundamental ro-vibrational transitions in this region. In addition, atmospheric water opacity, and therefore interference, is reduced in the 3–5 and 8–12 μm windows (respectively also referred as mid wave infrared – MWIR – and long wave infrared – LWIR); this proves advantageous for ground-based astronomy and remote atmospheric sounding in particular [7].

Whilst mid-IR spectrometers, interferometers, and sensing systems currently rely on open space optics, development of low cost mass-producible IO components would be transformative to enable full exploitation of the benefits of this spectral region. Silicon photonics has thus far provided the basis for mid-IR IO, taking advantage of mature micro-electronics foundry mask-etch processes for wafer-scale, high-quantity fabrication [8]. These techniques are costly and therefore high-risk for prototype device study, and are highly transmissive only in the MWIR water window. Suitable alternative materials for transmission over the full mid-IR window, including MWIR and LWIR, are chalcogenides, which

demonstrate low-losses (< 1 dB/cm) when processed via mask-etch techniques to produce planar waveguides [9].

Ultrafast laser inscription (ULI) has been demonstrated to produce low-loss (< 1 dB/cm) single-mode waveguides in chalcogenide glasses in the mid-IR [10], with the additional advantage of allowing out-of-plane three-dimensional (3D) inscription [11]. Recently, we demonstrated waveguides fabricated by ULI in $\text{Ge}_{33}\text{As}_{12}\text{Se}_{55}$ chalcogenide glass (also known by its commercial name IG2) [12] at $7.85 \mu\text{m}$ [13] in the LWIR with excellent refractive index contrast. In this work, we demonstrate and study IG2 evanescent field directional couplers operating in the LWIR for tailored beam splitting or combining; these simple structures provide the basis for future 3D mid-IR IO devices such as photonic lanterns, or sensing and spectroscopy devices that rely on interferometry and/or sample/reference channel comparison.

2. Device fabrication

Evanescent field couplers were fabricated in IG2 following an extensive waveguide test and characterization exercise, described in detail elsewhere [13]. The ULI fabrication parameter space was investigated such that the parameters required to fabricate single-mode straight waveguides, operating at $7.85 \mu\text{m}$ with known refractive index modification, were identified. The fabrication parameters are summarized in Table 1.

Table 1. ULI Parameters for Evanescent Field Couplers

Parameter	Value	Parameter	Value
Pulse energy	12.58 nJ	Inscription speed	10 mm/s
Inscription wavelength	1030 nm	Horizontal width	$19.8 \mu\text{m}$ (66 scans)
Pulse duration	355 fs	Vertical width	$\approx 15 \mu\text{m}$
Repetition rate	500 kHz	Multi-scan separation	$0.3 \mu\text{m}$
Inscription lens	0.55 NA		
Bulk refractive index (at $7.85 \mu\text{m}$) [14]	2.5032	Estimated modified refractive index [13]	≈ 2.5145

Use of these fabrication parameters led to waveguides with single-mode propagation characteristics, propagation losses of ≈ 1 dB/cm at $7.85 \mu\text{m}$, and estimated modified refractive index of 2.5145 [13]. Following the methodology of the test reported in [13], a further test IG2 chip containing waveguide bends was fabricated, using the above ULI parameters, to identify the optimum bend length L_B and bend width A for single-mode output, low-loss waveguide bends. L_B and A define the sine-squared form of the waveguide bend [15], described in Eq. (1) and Fig. 1. A was varied from 40 to $130 \mu\text{m}$, and L_B from 2 to 9 mm, based on numerical modeling using FIMMPROP optical propagation modeling software. The results were inconclusive, as the bend introduced relatively small additional losses compared with the manufacturing repeatability achieved for these waveguides [16]. As the choice of parameters were found not critical, bends in the center of this parameter space, with $L_B = 4$ mm and $A = 100 \mu\text{m}$, were chosen for demonstration of couplers.

$$x(z) = A \sin^2 \left(\frac{2\pi z}{4L_B} \right). \quad (1)$$

The form of the fabricated couplers is shown in Fig. 1, which also defines the x and z directions. Sine-squared bends of the form described in Eq. (1) link the input ports P_1 and P_2 to the interaction region. The interaction length L_I was varied; the full length of each coupler was 20 mm, and the center of L_I kept at the center of the chip, with the length of straight waveguide sections at the input and output ports varied to ensure the waveguides reached the edges of the chip. In this instance, the waveguide core-to-core separation d was kept constant at $19.8 \mu\text{m}$; this means the two waveguides are immediately adjacent to one another in the interaction region.

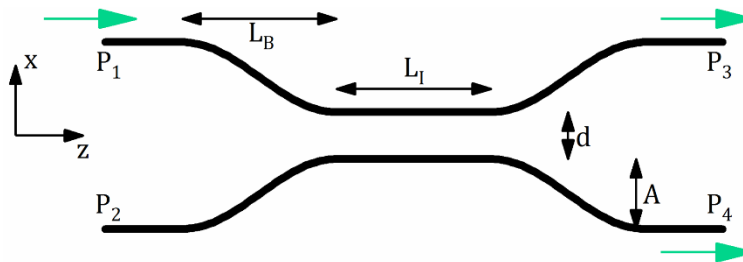


Fig. 1. Schematic of fabricated couplers (not to scale). Light input at port P_1 was measured at output ports P_3 and P_4 . Bend length L_B and bend width A were kept constant. Interaction length L_I was varied, and the lengths of the straight input arms at either end of the waveguide changed to compensate. The mid-point of L_I was kept in the center of the waveguide chip. Waveguide separation d was kept constant.

Figure 2 shows microscope images of fabricated couplers. The facet profile in Fig. 2(a) shows that the waveguides are rectangular in form, with vertical cross-section approx. $15\ \mu\text{m}$; this is defined by the laser inscription parameters (depth of focus), and is not actively controlled during the fabrication process. Figure 2(b) shows the input bend (left) and interaction regions (right) of a coupler from the top surface of the waveguide chip. The waveguides meet on the right-hand edge of the figure as expected. These images were taken using a Leitz Ergolux microscope and a standard DSLR camera with the IR filter removed.

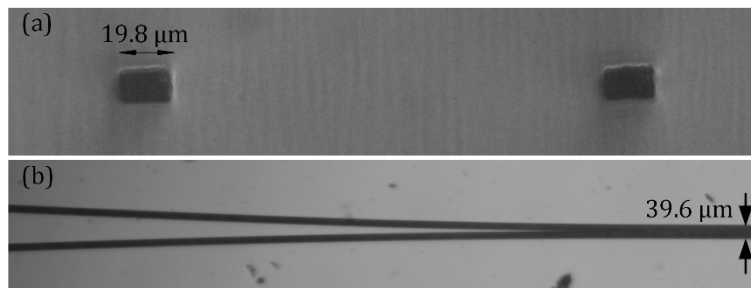


Fig. 2. Microscope images of fabricated couplers. (a) Facet image, showing two coupled waveguide ports. (b) Top image of coupler, showing bend (left) into interaction region (right).

3. Coupler experimental characterization

Waveguides were characterized using the setup outlined in Fig. 3. The laser was an Alpes Lasers S.A. quantum cascade laser (QCL) with output at $7.85\ \mu\text{m}$, operated using a Cascade Technologies Ltd. LM-01 air-cooled housing. The laser was coupled to the waveguide using a microscope objective (MSC1), which created an approx. $10\ \mu\text{m}$ beam waist at the waveguide facet. The output of the coupler was imaged onto an Electrophysics PV320 camera, at position 'A', and background-normalized images of the coupler throughput were taken. All data presented were taken with light polarized in the same plane as the coupler bends; by virtue of the geometry, this 'TE' polarization state will be most affected by the horizontal bend and coupler structure.

Figure 4 shows measured output profiles for a range of fabricated couplers. In all cases, light was input at port P_1 , and the through-port P_3 output is on the left of each image. The interaction length L_I varies between 1.4 mm and 2.4 mm, and the coupling ratio is observed to change as L_I changes. The full range of $> 99\%$ coupling into the through-port P_3 , and $> 99\%$ coupling into the coupled-port P_4 was observed.

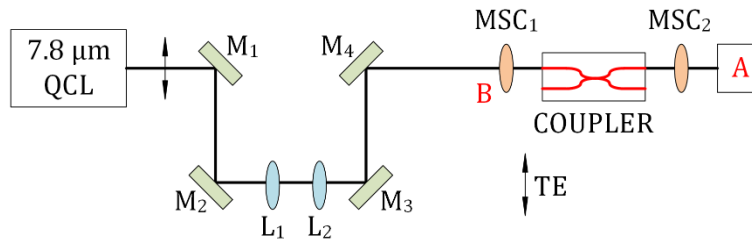


Fig. 3. Schematic of characterization setup. The laser output is incident on beam-steering mirrors M_1 – M_4 , and lenses L_1 and L_2 ensure the beam incident on MSC_1 has 1.5 mm beam waist radius. MSC_1 couples the resulting beam into the waveguide, and MSC_2 is used to collect the output image onto a camera or power meter at position ‘A’. Position ‘B’ is the position of the power meter for throughput power observation.

The through-port coupling ratio was calculated by fitting a 2D-Gaussian profile to each individual waveguide output in the plots obtained in Fig. 4, and calculating the volume contained under the fitted curve. This allowed the normalized intensity at the output of each coupler arm to be observed. The through-port coupling ratio was then calculated using the relation $P_3 / (P_3 + P_4)$. For couplers where no output was observed at one of the ports, e.g., Figs. 4(a) and 4(e), the coupling ratio was normalized to one or zero, for 100% through-port (P_3) or 100% coupled-port (P_4), respectively. These data are shown in Fig. 5, as blue points. The L_I cycle length was 2.277 mm, calculated via the sine-squared fit to the data.

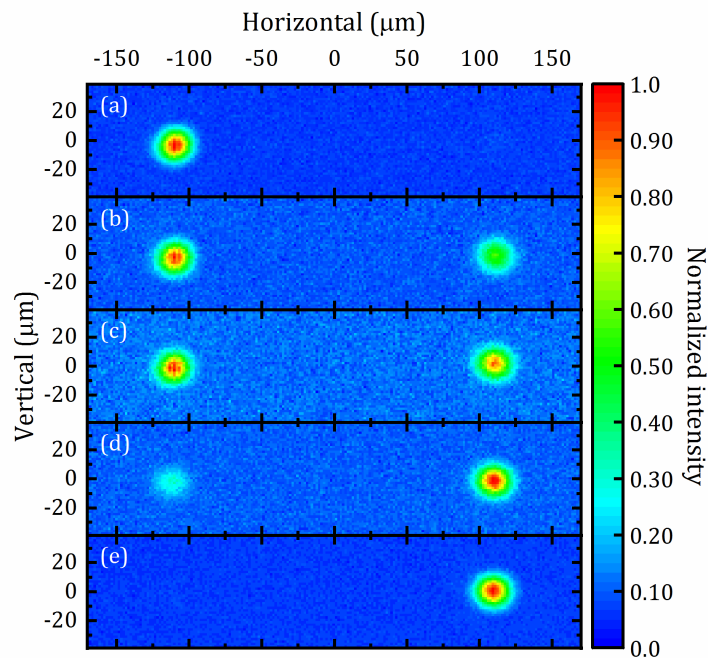


Fig. 4. Normalized output profiles from the evanescent field couplers, with interaction lengths: (a) 1.4 mm; (b) 1.8 mm; (c) 2.0 mm; (d) 2.2 mm; and (e) 2.4 mm. Length scales are normalized via the magnification of the characterization setup such that image dimensions are scaled to the chip facet dimensions.

Error bars in Fig. 5 are dominated by the manufacturing repeatability, and were obtained by duplicating a subset of couplers with identical manufacturing conditions on the same waveguide chip. Each coupler was characterized, and the through-port coupling ratios for duplicates compared; the average of these values was taken as an estimate of the

manufacturing repeatability, which was ± 0.049 . It should be noted that these values contain not only manufacturing repeatability variation, but also small contributions from measurement repeatability and Gaussian fitting errors; detailed description of these errors is presented elsewhere [13], and manufacturing repeatability was found to dominate significantly.

In addition to repeatability errors, reciprocity of the couplers was investigated. This is the comparison of the through-port coupling ratio measured when input is into port P_1 (P_3 output) or P_2 (P_4 output). The reciprocity was found to be within ± 0.029 across the couplers measured. The reciprocity is a direct result of manufacturing repeatability error, as any difference in the propagation constants of the input waveguides P_1 and P_2 will introduce changes to the coupling ratio observed at the waveguide output. The proximity of the coupler arms in and surrounding L_I during fabrication may cause an enhanced refractive index modification in one waveguide compared to the other, contributing to this mismatch in propagation constants.

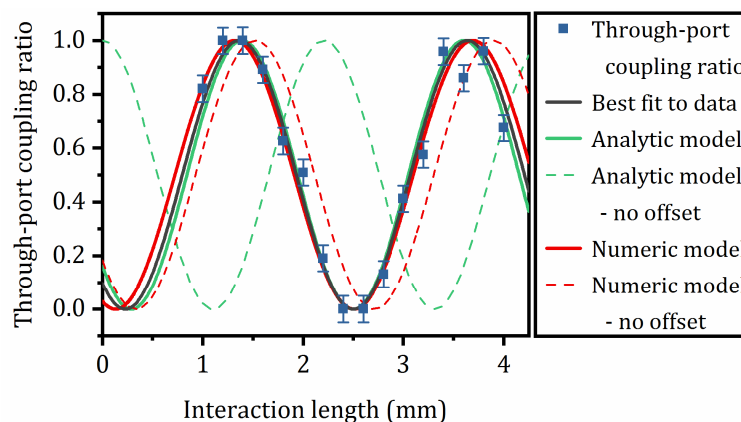


Fig. 5. Through-port coupling ratio (blue points) for changing L_I , for $d = 19.8 \mu\text{m}$ center-to-center waveguide separation. The analytic model (green lines) and numeric model (red lines) are also shown, alongside the sine-squared fit to the measured data (black line).

In addition to the couplers, an array of straight waveguides was fabricated on chip, for initial alignment and to determine loss characteristics. The propagation loss of the straight waveguides was found to be ≈ 1 dB/cm; the method of measurement and calculation is described in more detail elsewhere [13]. Due to the large-area power meter used (Ophir 3A, 9.5 mm aperture), a direct measurement of the power at each output port of the coupler was not possible without implementing a micro-metrically controlled beam stop. Instead, the relative output power of a straight waveguide and combined output power of the couplers was inferred from the intensity measurements made using the camera, which is more precise a measurement.

Under identical conditions of illumination and fabrication, the transmitted power reference from a straight waveguide was measured. The chip position was then re-adjusted to couple and measure successively 14 coupler outputs. The total power output at the end of a coupler was, on average, 82% of that of a straight waveguide. This implies that the total loss of the device consists of ≈ 1 dB/cm propagation loss, and 0.9 dB insertion loss. The insertion loss comprises all additional losses caused by the coupler compared to a straight waveguide, including bend and radiation losses. This loss does not include input and output coupling losses or Fresnel reflections.

4. Coupler modelling

Verification of the performance of these couplers was done by comparison to analytic and numeric models of the structure. The analytic model is described in detail in the literature [17], and applies to the general case of coupled co-directional waveguides along the straight interaction length L_I only, with the waveguides assumed to be identical (identical propagation constants). In short, for the case where 100% of the input light is coupled to one input port of the coupler, the power in that through-arm for a specific interaction length is governed by Eq. (2). The power in the coupled-arm is the complementary.

$$P_t(z) = 1 - \sin^2(\kappa L_I + \phi). \quad (2)$$

κ is the mode coupling coefficient of the coupler, for the fundamental TE mode of the input waveguide. As our couplers consist not only of the straight interaction length L_I , but also evanescently-coupled bend regions, we introduce an additional dimensionless phase term $\phi = \kappa \times l_{eff}$ to account for the effective additional coupling length l_{eff} in the coupler geometry. κ is dependent on the refractive index modification, physical dimensions of the coupler, and operating wavelength, and can be obtained numerically as presented in Eq. (3).

$$\kappa = \frac{\sqrt{2\Delta} (k_x a)^2 (\gamma_x a)^2}{a (1 - \gamma_x a) \nu^3} \exp[-\gamma_x (d - 2a)]. \quad (3)$$

Δ is the dimensionless refractive index modification produced by ULI, a is the waveguide half-width, ν is the normalized frequency, and k_x and γ_x are transversal wavenumbers, obtained following Marcatili's method [17]. In our case, $d = 2a$, so the exponential term disappears.

Table 2. Comparison of Measured and Modelled Couplers

Parameter	Measured	Analytic model	Numeric model
κ	$1.380 \pm 0.027 \text{ mm}^{-1}$	1.423 mm^{-1}	1.323 mm^{-1}
cycle length = π/κ	2.277 mm	2.208 mm	2.375 mm
l_{eff}	-	0.812 mm	0.203 mm

Figure 5 shows the best-fit to the measured data (black) and analytically calculated (solid green) curves governed by the parameters presented in Table 2. There is good agreement between the measured and calculated data, with calculated κ only 3% higher than measured, and only 69 μm difference between the predicted and measured cycle length. The model does require an additional effective length l_{eff} of 0.812 mm to achieve agreement with the measured data (model without ϕ is shown in dashed green). The uncertainties on the calculated κ from waveguide parameters come mostly from the ULI-modified refractive index (0.001) and the inscription length uncertainties (0.2 μm). These propagate as respectively 0.035 and 0.046 mm^{-1} , giving a sum of square uncertainty of 0.058 mm^{-1} . Besides the over-simplistic collinear straight waveguides, the model assumes $|E_x| \gg |E_y|$ for the fundamental TE mode, which simplifies the calculation such that the vertical extent of the waveguide is omitted from the calculation. While true in the general square waveguide case, it is likely that the rectangular waveguide form observed in Fig. 2(a) will cause some change to the mode coupling coefficient compared to that of a square waveguide, which will therefore contribute to the error in cycle length observed. With these caveats, the measurements do agree well with the analytical expectations.

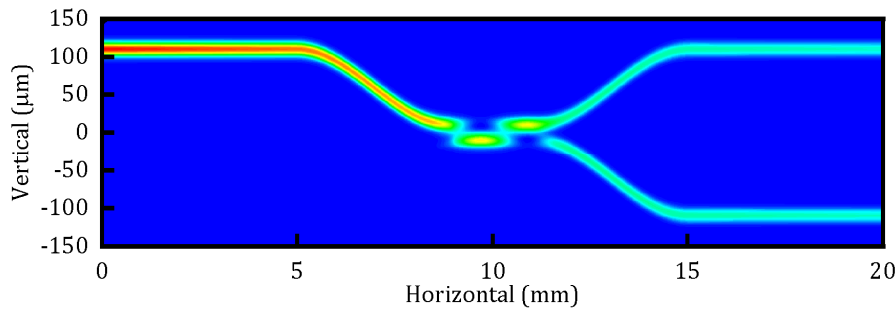


Fig. 6. Field intensity modelled by FIMMPROP in the IG2 coupler under the condition of $L_t = 2.117$ mm, for 50:50 coupling.

In addition, a numeric model based on the real coupler geometry was developed in FIMMPROP, using the same waveguide parameters as input to the analytic model. κ was found to be 1.323 mm^{-1} , which is 4.1% lower than derived from the data. The numerical model is shown in Fig. 5 (solid red line), and the simulated field propagation in Fig. 6. The sine-squared fit describing the numeric model output requires $l_{eff} = 0.203$ mm offset for the least-squared difference best-fit to the data. As expected for this numeric model, which does take into account the bend regions of the coupler, the model requires much smaller correction l_{eff} than the analytic model to achieve agreement with the measured data. However, the fact a small correction is still required further demonstrates the effect of fabrication uncertainties on the coupler output. Both numeric and analytic models agree well with the measurement, within these bounds.

5. Conclusion

In conclusion, we have presented the first demonstration of evanescent field LWIR couplers in IG2 chalcogenide glass, with demonstrated coupling ratios between 0 and 100% into the coupled-port output at $7.85 \mu\text{m}$. Additional insertion loss of the device compared to straight waveguides was estimated to be around 0.9 dB, in addition to ≈ 1 dB/cm waveguide propagation loss. Comparison of the measured couplers to both simplified analytic and full geometry numeric models resulted in good agreement between the mode coupling coefficient and cycle length, considering the known fabrication uncertainties. The ULI IG2 evanescent field coupler provides a significant step toward mid- and long-wave IR photonic devices, including 3-D beam combiners such as photonic lanterns, and evanescent sensing devices based on Mach-Zehnder interferometers.

Funding

Science and Technology Facilities Council (STFC) Center for Instrumentation, UK; STFC Consortium Grant ST/N000625/1, UK; Engineering and Physical Sciences Research Council Grant EP/K030884/1), UK

Acknowledgments

We thank the Precision Development Facility, RAL Space, for manufacture of characterization components.

References

1. H. Takahashi, S. Suzuki, K. Kato, and I. Nishi, "Arrayed-waveguide grating for wavelength division multi/demultiplexer with nanometre resolution," *Electron. Lett.* **26**(2), 87–88 (1990).
2. P. Dumais, C. L. Callender, J. P. Noad, and C. J. Ledderhof, "Silica-on-silicon optical sensor based on integrated waveguides and microchannels," *IEEE Photon. Technol. Lett.* **17**(2), 441–443 (2005).
3. A. Politi, M. J. Cryan, J. G. Rarity, S. Yu, and J. L. O'Brien, "Silica-on-silicon waveguide quantum circuits," *Science* **320**(5876), 646–649 (2008).

4. J. Kasberger, T. Fromherz, A. Saeed, and B. Jakoby, "Miniaturized integrated evanescent field IR-absorption sensor: Design and experimental verification with deteriorated lubrication oil," *Vib. Spectrosc.* **56**(2), 129–135 (2011).
5. V. M. Lavchiev and B. Jakoby, "Photonics in the mid-infrared: challenges in single-chip integration and absorption sensing," *IEEE J. Sel. Top. Quantum Electron.* **23**(2), 8200612 (2017).
6. H. K. Hsiao, K. A. Winick, J. D. Monnier, and J.-P. Berger, "An infrared integrated optic astronomical beam combiner for stellar interferometry at 3-4 microm," *Opt. Express* **17**(21), 18489–18500 (2009).
7. I. S. Glass, *Handbook of Infrared Astronomy* (Cambridge University, 1999).
8. R. Soref, "Toward silicon-based longwave integrated optoelectronics (LIO)," *Proc. SPIE* **6898**, 689809 (2008).
9. N. Hô, M. C. Phillips, H. Qiao, P. J. Allen, K. Krishnaswami, B. J. Riley, T. L. Myers, and N. C. Anheier, Jr., "Single-mode low-loss chalcogenide glass waveguides for the mid-infrared," *Opt. Lett.* **31**(12), 1860–1862 (2006).
10. A. Ródenas, G. Martin, B. Arezki, N. Psaila, G. Jose, A. Jha, L. Labadie, P. Kern, A. Kar, and R. Thomson, "Three-dimensional mid-infrared photonic circuits in chalcogenide glass," *Opt. Lett.* **37**(3), 392–394 (2012).
11. R. R. Thomson, R. J. Harris, T. A. Birks, G. Brown, J. Allington-Smith, and J. Bland-Hawthorn, "Ultrafast laser inscription of a 121-waveguide fan-out for astrophotonics," *Opt. Lett.* **37**(12), 2331–2333 (2012).
12. "Vitron IG2 datasheet," <http://www.vitron.de/english/IR-Glaeser/Daten-Infrarotglaeser.php>.
13. H. L. Butcher, D. G. MacLachlan, D. Lee, R. R. Thomson, and D. Weidmann, "Demonstration and characterization of ultrafast laser-inscribed mid-infrared waveguides in chalcogenide glass IG2," *Opt. Express* **26**(8), 10930–10943 (2018).
14. M. N. Polyanskiy, "Optical constants of Vitron IG2," <https://refractiveindex.info/?shelf=glass&book=VITRON-IG&page=IG2>.
15. A. Arriola, S. Mukherjee, D. Choudhury, L. Labadie, and R. R. Thomson, "Ultrafast laser inscription of mid-IR directional couplers for stellar interferometry," *Opt. Lett.* **39**(16), 4820–4822 (2014).
16. H. L. Butcher, D. Lee, D. Weidmann, D. G. MacLachlan, and R. R. Thomson, "Ultrafast laser-inscribed waveguides in IG2 chalcogenide glass for mid-infrared photonics applications," *Proc. SPIE* **10535**, 1053514 (2018).
17. K. Okamoto, *Fundamentals of Optical Waveguides*, 2nd ed. (Academic, 2006).